Monthly Notices of the ROYAL ASTRONOMICAL SOCIETY

MNRAS **527,** 4899–4912 (2024) https://doi.org/10.1093/mnras/stad3225
Advance Access publication 2023 October 21

ExoMol line lists – LIII: empirical rovibronic spectra of yttrium oxide

Sergei N. Yurchenko [1], Ryan P. Brady,[1] Jonathan Tennyson [1]★ Alexander N. Smirnov,[2] Oleg A. Vasilyev[3] and Victor G. Solomonik[2]

[1]*Department of Physics and Astronomy, University College London, Gower Street, WC1E 6BT London, UK*
[2]*Department of Physics, Ivanovo State University of Chemistry and Technology, Sheremetev Ave., 7, Ivanovo 153000, Russia*
[3]*Department of Chemistry and Biochemistry, The Ohio State University, Columbus, OH 43210, USA*

Accepted 2023 October 17. Received 2023 October 16; in original form 2023 August 7

ABSTRACT

Empirical line lists BRYTS for the open shell molecule $^{89}Y^{16}O$ (yttrium oxide) and its isotopologues are presented. The line lists cover the six lowest electronic states: $X\,^2\Sigma^+$, $A\,^2\Pi$, $A'\,^2\Delta$, $B\,^2\Sigma^+$, $C\,^2\Pi$, and $D\,^2\Sigma^+$ up to 60 000 cm^{-1} (<0.167 μm) for rotational excitation up to $J = 400.5$. An *ab initio* spectroscopic model consisting of potential energy curves (PECs), spin–orbit, and electronic angular momentum couplings is refined by fitting to experimentally determined energies of YO, derived from published YO experimental transition frequency data. The model is complemented by empirical spin-rotation and Λ-doubling curves and *ab initio* dipole moment and transition dipole moment curves computed using multireference configuration interaction (MRCI). The *ab initio* PECs computed using the complete basis set limit extrapolation and the coupled-cluster CCSD(T) method with its higher quality provide an excellent initial approximation for the refinement. Non-adiabatic coupling curves for two pairs of states of the same symmetry *A*/*C* and *B*/*D* are computed using a state-averaged complete active space self-consistant field theory (CASSCF) and used to build diabatic representations for the $A\,^2\Pi$, $C\,^2\Pi$, $B\,^2\Sigma^+$, and $D\,^2\Sigma^+$ curves. The experimentally derived energies of $^{89}Y^{16}O$ utilized in the fit are used to replace the corresponding calculated energy values in the BRYTS line list. Simulated spectra of YO show excellent agreement with the experiment, where it is available. Calculated lifetimes of YO are tuned to agree well with the experiment, where available. The BRYTS YO line lists are available from the ExoMol database (www.exomol.com).

Key words: molecular data – exoplanets – stars: atmospheres – stars: low-mass.

1 INTRODUCTION

The spectrum of yttrium oxide, YO, has been the subject of many astrophysical studies. It has been observed in the spectra of cool stars (Wyckoff & Clegg 1978) including R-Cygni (Sauval 1978; Murty 1982), Pi-Gruis (Murty 1983), V838 Mon (Goranskii & Barsukova 2007; Kaminski et al. 2009), and V4332 Sgr (Goranskii & Barsukova 2007; Tylenda et al. 2015). YO has also been actively used in laser cooling experiments (Yeo et al. 2015; Collopy et al. 2015; Quéméner & Bohn 2016; Collopy et al. 2018). Its spectrum has been used as a probe to study high-temperature materials (Badie, Cassan & Granier 2005a).

There are many laboratory spectroscopic studies of YO, including its $A\,^2\Pi - X\,^2\Sigma^+$ (Shin & Nicholls 1977; Linton 1978; Bernard, Bacis & Luc 1979; Liu & Parson 1979; Wijchers et al. 1980; Bagare & Murthy 1982; Bernard & Gravina 1983; Wijchers et al. 1984; Childs, Poulsen & Steimle 1988; Steimle & Shirley 1990; Dye, Muenchausen & Nogar 1991; Fried et al. 1993; Otis & Goodwin 1993; Badie & Granier 2002, 2003; Badie, Cassan & Granier 2005a; Badie, Cassan & Granier 2005b; Kobayashi & Sekine 2006; Badie, Cassan & Granier 2007a; Badie et al. 2007b; Collopy et al. 2015; Mukund & Nakhate 2023), $B\,^2\Sigma^+ - X\,^2\Sigma^+$ (Shin & Nicholls 1977; Bernard, Bacis & Luc 1979; Bernard & Gravina 1980; Fried et al. 1993; Leung, Ma & Cheung 2005; Zhang et al. 2017), $A'\,^2\Delta - X\,^2\Sigma^+$(Chalek & Gole 1976; Simard et al. 1992; Collopy et al. 2015) and $D\,^2\Sigma^+ - X\,^2\Sigma^+$ (Zhang et al. 2017) band systems, rotational spectrum (Uhler & Akerlind 1961; Steimle & Alramadin 1986; Hoeft & Torring 1993), hyperfine spectrum (Kasai & Weltner 1965; Steimle & Alramadin 1986, 1987; Childs, Poulsen & Steimle 1988; Suenram et al. 1990; Knight et al. 1999; Steimle & Virgo 2003), and chemiluminescence spectra (Manos & Parson 1975; Chalek & Gole 1977; Fried et al. 1993). The very recent experimental study of the $A\,^2\Pi$ and $B\,^2\Sigma^+$ systems of YO by Mukund & Nakhate (2023) provided crucial information for this work on the coupling between the $B\,^2\Sigma^+$ and $D\,^2\Sigma^+$ states. Relative intensity measurements of the $A\,^2\Pi - X\,^2\Sigma^+$ system were performed by Bagare & Murthy (1982). Permanent dipole moments of YO in both the $X\,^2\Sigma^+$ and $A\,^2\Pi$ states have been measured using the Stark technique (Steimle & Shirley 1990; Suenram et al. 1990; Steimle & Virgo 2003). The lifetimes in the $A\,^2\Pi$, $B\,^2\Sigma^+$, and $D\,^2\Sigma^+$ states were measured by Liu & Parson (1977) and Zhang et al. (2017).

Our high-level *ab initio* study (Smirnov et al. 2019) forms a pre-requisite for this work, where a mixture of multireference configuration interaction (MRCI) and coupled cluster methods were used to produce potential energy curves (PECs), spin–orbit curves

★ E-mail: j.tennyson@ucl.ac.uk

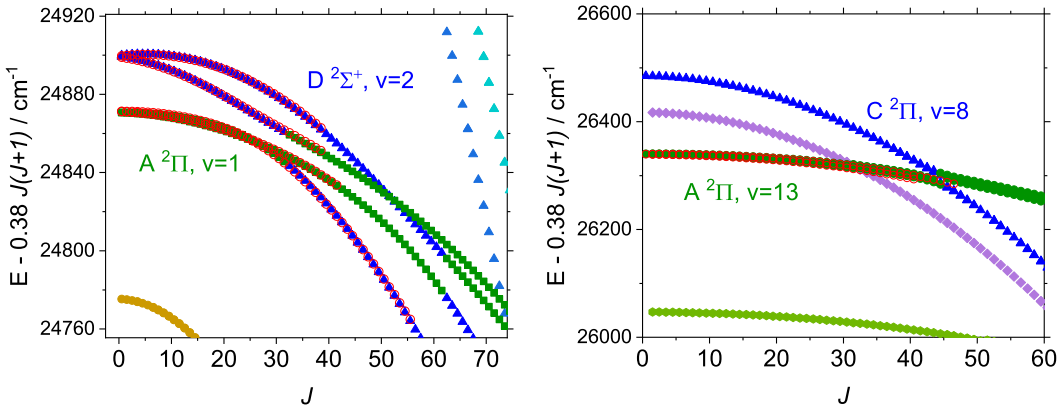

Figure 1. Illustration of the crossings: $D\,^2\Sigma^+$, $v = 2$ and $A\,^2\Pi$, $v = 11$ bands (left); $A\,^2\Pi$, $v = 13$ and $C\,^2\Pi$, $v = 8$ (right). The experimental values are shown as empty circle.

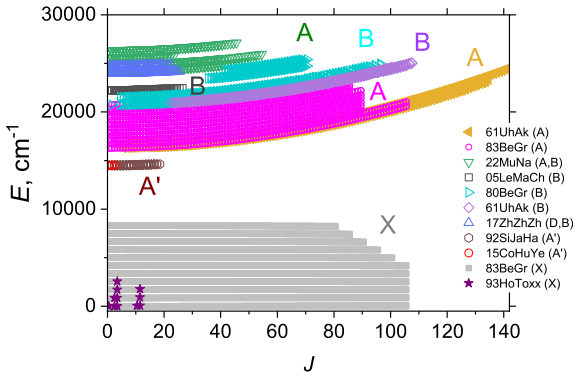

Figure 2. Experimentally derived energy term values of YO used in the refinement of the *ab initio* spectroscopic model.

(SOCs), electronic angular momentum curves (EAMCs), electric dipole moment curves (DMCs), and transition dipole moment curves (TDMCs) covering the six lowest electronic states of YO. Other theoretical studies of YO include MRCI calculations by Langhoff & Bauschlicher (1988) and complete active space second-order perturbation theory (CASPT2) calculations of spectroscopic constants by Zhang et al. (2017).

In this paper, the *ab initio* spectroscopic model of Smirnov et al. (2019) is extended by introducing non-adiabatic coupling (NAC) curves for two pairs of states, *A*/*C* and *B*/*D*, and then refined by fitting to experimentally derived energies of YO using our coupled-states nuclear-motion program DUO (Yurchenko et al. 2016). The energies are constructed using a combination of the spectroscopic constants and line positions taken from the literature through a procedure based on the MARVEL (Measured Active Rotational Vibrational Energy Levels, Furtenbacher, Császár & Tennyson 2007) methodology. The new empirical spectroscopic model is used to produce the hot line list BRYTS for three major isotopologues of YO, $^{89}Y^{16}O$, $^{89}Y^{17}O$, and $^{89}Y^{18}O$ as part of the ExoMol project (Tennyson & Yurchenko 2012; Tennyson et al. 2020).

2 EXPERIMENTAL INFORMATION

Although the spectroscopy of YO has been extensively studied, some key high-resolution experimental sources from the 1970–1980s only provide spectroscopic constants rather than original transition frequencies; this limits their usability for high-resolution applications. For cases where only spectroscopic constants are available we used an effective Hamiltonian model to compute the corresponding energy term values. This includes term values for the ground electronic $X\,^2\Sigma^+$ state. In the following, experimental studies of YO are reviewed.

61UhAk: Uhler & Akerlind (1961) reported line positions from the $B\,^2\Sigma^+$–$X\,^2\Sigma^+$ (0,0) and $A\,^2\Pi$–$X\,^2\Sigma^+$ (0,0) bands, but the $B\,^2\Sigma^+$–$X\,^2\Sigma^+$ band is fully covered by more recent and accurate data (Bernard & Gravina 1980). The quantum numbers F_1 and F_2 of $B\,^2\Sigma^+$–$X\,^2\Sigma^+$ had to be swapped to agree with Bernard & Gravina (1980). However, due to many conflicting combination differences, only high J transitions ($J > 100.5$) were included in our final analysis.

77ShNi: Shin & Nicholls (1977) performed an analysis of the blue-green $B\,^2\Sigma^+$–$X\,^2\Sigma^+$ and orange $A\,^2\Pi$–$X\,^2\Sigma^+$ systems but no rovibronic assignment was reported and their data are not used here.

79BeBaLu: Bernard, Bacis & Luc (1979) reported an extensive analysis of the A–X ($v' = 0, 1, 2, 3, 4, 5$) and B–X ($v' = 0, 1$) systems. Only spectroscopic constants were reported. This work has been superseded by more recent studies and therefore is not used here.

80BeGr: Bernard & Gravina (1980) reported line positions from the $B\,^2\Sigma^+$–$X\,^2\Sigma^+$ system, $v' = 0, 1$ and $v'' = 0, 1, 2, 3$ and spectroscopic constants for $v' = 0, 1, 2, 3$, in emission in a hollow cathode discharge with a partial analysis of the (3,2) and (4,3) bands (only higher $J \geq 35.5$ and $J \geq 57.5$, respectively). The data were included in our analysis.

83BeGr: Bernard & Gravina (1983) presented a study of the $A\,^2\Pi$–$X\,^2\Sigma^+$ system of YO excited in the discharge of a hollow cathode tube. Only spectroscopic constants were reported, covering the $X\,^2\Sigma^+$ ($v = 0,\ldots,10$) and $A\,^2\Pi$ ($v = 0,\ldots,9$) vibronic states ($v = 6$ and 7 with a limited analysis). We used these constants and the effective Hamiltonian of Bacis et al. (1977) to generate term values for the states $v = 0, \ldots, 5, 8$, and 9 ($A\,^2\Pi$). It should be noted that the spectroscopic program PGOPHER (Western 2017) could not be used as its $^2\Pi$ model is found to be incompatible with that used by Bernard & Gravina (1983) despite constants sharing the same names. A simple PYTHON code based on the effective Hamiltonian expressions of Bacis et al. (1977) is provided as part of our Supporting Information. Band heads of $v' = 7$–15 ($\Omega = 0.5$) and $v' = 6, 8, 9$ ($\Omega = 1.5$) were reported, but not used directly in the fit here. It is known that effective Hamiltonian expansions can diverge at high J, we therefore limited the corresponding energies to about $J \leq 100.5$.

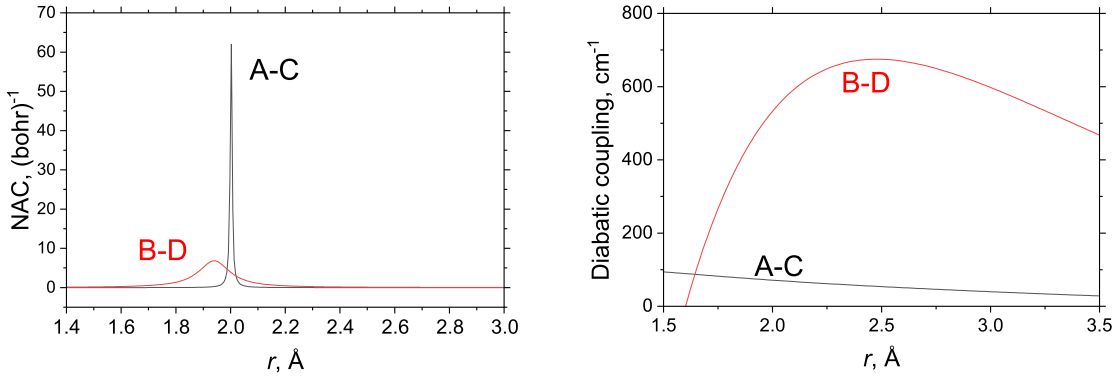

Figure 3. CASSCF NACs and empirical diabatic couplings $D(r)$ of YO, A–C, and B–D.

The coverage of the spectroscopic constants of $X\,^2\Sigma^+$ is up to $v = 10$, while the available line positions are only up to $v = 3$, which is why we opted to use the spectroscopic constants by Bernard & Gravina (1983) to generate the $X\,^2\Sigma^+$ term values. YO has a relatively rigid structure in its ground electronic state potential with the vibronic energies well separated from each other and other electronic state.

92SiJaHa: Simard et al. (1992) reported line positions from the $A'\,^2\Delta$–$X\,^2\Sigma^+$ system (0,0) in their laser-induced fluorescence spectral study with a pulsed dye laser. It was included in the analysis here.

93HoTo: Hoeft & Torring (1993) reported a microwave spectrum of $X\,^2\Sigma^+$ for $v = 0, 1, 2, 3$. It was included in the analysis here.

05LeMaCh: Leung, Ma & Cheung (2005) reported a cavity ring-down absorption spectrum of the $B\,^2\Sigma^+$–$X\,^2\Sigma^+$ (2,0) and (2,1) system. We included their line positions in the analysis here.

15CoHuYe: Collopy et al. (2015) reported three THz lines from the $A\,^2\Pi$–$X\,^2\Sigma^+$ (0,0) system with low uncertainties recorded for laser cooling application. These were included in our analysis.

17ZhZhZh: Zhang et al. (2017) reported line positions from the $D\,^2\Sigma^+$–$X\,^2\Sigma^+$ system (0,0) and (1,0) which were used in the analysis here.

23MuNa: Mukund & Nakhate (2023) reported a high-resolution analysis of the highly excited $A\,^2\Pi$–$X\,^2\Sigma^+$ ($v' = 11$, 12, 13) and $B\,^2\Sigma^+$–$X\,^2\Sigma^+$ ($v' = 5$, 6) systems. For the A–X band, only the $\Omega = 0.5$ branch was provided. Their line positions were included in our analysis. There is a crossing between $A\,^2\Pi$, $v = 11$ and $D\,^2\Sigma^+$, $v = 2$ around $J = 34.5$; see Fig. 1.

The only experimental information on the transition probabilities available for YO includes the permanent dipole moments in the $X\,^2\Sigma^+$ and $A\,^2\Pi$ states measured by Steimle & Shirley (1990), Suenram et al. (1990), Steimle & Virgo (2003) and the lifetimes of some lower lying vibrational states measured by Liu & Parson (1977) ($A\,^2\Pi$) and Zhang et al. (2017) ($B\,^2\Sigma^+$ and $D\,^2\Sigma^+$).

3 DESCRIPTION OF THE PSEUDO-MARVEL PROCEDURES

MARVEL is a spectroscopic network algorithm (Furtenbacher, Császár & Tennyson 2007), now routinely used for constructing ExoMol line lists for high-resolution applications (Tennyson et al. 2020). We did not have sufficient original experimental line positions for a proper MARVEL analysis of the YO spectroscopic data, which were mostly only available represented by spectroscopic constants. Furthermore, there are no studies of the infrared (IR) spectrum of YO which meant that the (lower) ground energies could be only reconstructed from lower quality UV transitions, which limits the quality of the MARVEL energies.

Instead, a 'pseudo-MARVEL' procedure was applied as follows (see also Yurchenko et al. 2022). The experimental frequencies $\tilde{\nu}_{ij}$, where available, were utilized to generate rovibronic energies of YO as upper states energies using

$$\tilde{E}_{j(i)}^{(\mathrm{upp})} = \tilde{E}_i^{(\mathrm{low})} + \tilde{\nu}_{ij}, \tag{1}$$

which were then averaged over all transitions connecting the same upper state j. All experimental transitions originate from or end up at the $X\,^2\Sigma^+$ state. We used the spectroscopic constants from Bernard & Gravina (1983) ($v = 0, 1, \ldots, 10$) to generate the $X\,^2\Sigma^+$ state energies $\tilde{E}_i^{(\mathrm{low})}$ in conjunction with the program PGOPHER. The $A\,^2\Pi$ state energies were generated using the effective Hamiltonian (Bacis et al. 1977) except for $v = 0$, $J > 100.5$, which were obtained using the pseudo-MARVEL procedure. This pseudo-MARVEL analysis yielded 5089 empirically determined energy levels which we used in the fit. The final experimentally determined energy set covers the following vibronic bands X: $v = 0 - 10$; A': $v = 0$, $J_{\max} = 14.5$; A: $v = 0$,1,2,3,4,5, 8,9, 11,12,13; B: $v = 0$, 1, 2, 3, 4, 5, 6; and D: $v = 0$, 1. The vibrational and rotational coverage is illustrated in Fig. 2. The experimental transition frequencies collected as part of this work are provided in the Supporting Information to this paper in the MARVEL format together with the pseudo-MARVEL energies used in the fit.

It should be noted that the effective Hamiltonians used do not provide any information on direct perturbations between vibronic bands caused by their crossing or any other interband interactions. For example, the $A\,^2\Pi$ $v = 5$ and $B\,^2\Sigma^+$ $v = 0$ states cross at around $J = 27.5$. We excluded energy values in the vicinity of such crossings from the fit. The only crossing represented by the real data is between the $D\,^2\Sigma^+$ $v = 2$ and $A\,^2\Pi$ $v = 11$ bands (Mukund & Nakhate 2023), see Fig. 1.

4 *AB INITIO* CALCULATIONS

NACs or the first-order derivative couplings between the state pairs $X\,^2\Sigma^+ - B\,^2\Sigma^+$, $X\,^2\Sigma^+ - D\,^2\Sigma^+$, $B\,^2\Sigma^+ - D\,^2\Sigma^+$, and $A\,^2\Pi - C\,^2\Pi$ were derived by three-point central differences for CASSCF wavefunctions using the DDR procedure as implemented in MOLPRO (Werner et al. 2020). The state-averaged CASSCF method was employed with density matrix averaging over six low-lying doublet states (three Σ^+, two Π, and one Δ) with equal weights for each of the roots. The active space included 7 electrons distributed in 13 orbitals ($6a_1$, $3b_1$, $3b_2$, $1a_2$) that had pre-dominantly oxygen 2p and yttrium 4d, 5s, 5p, and 6s character; all lower energy orbitals were constrained

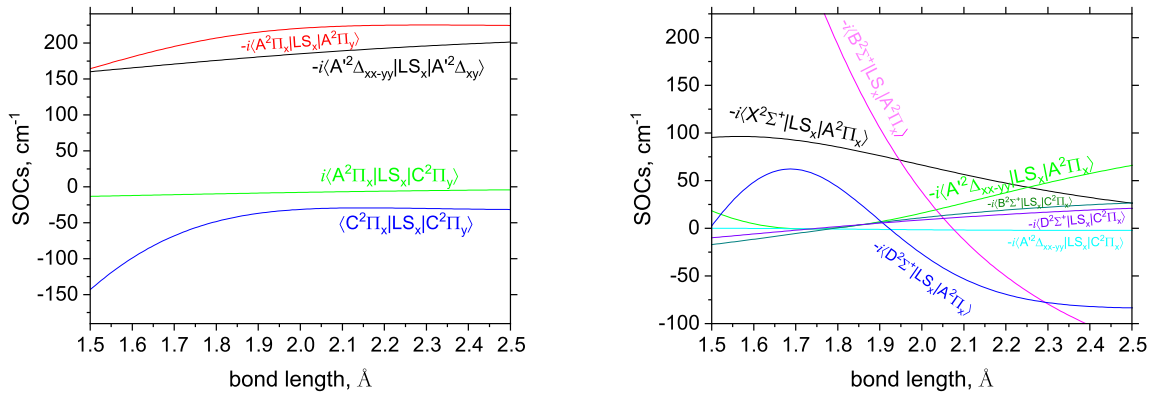

Figure 4. Refined SOCs of YO in the diabatic representation: diagonal and non-diagonal.

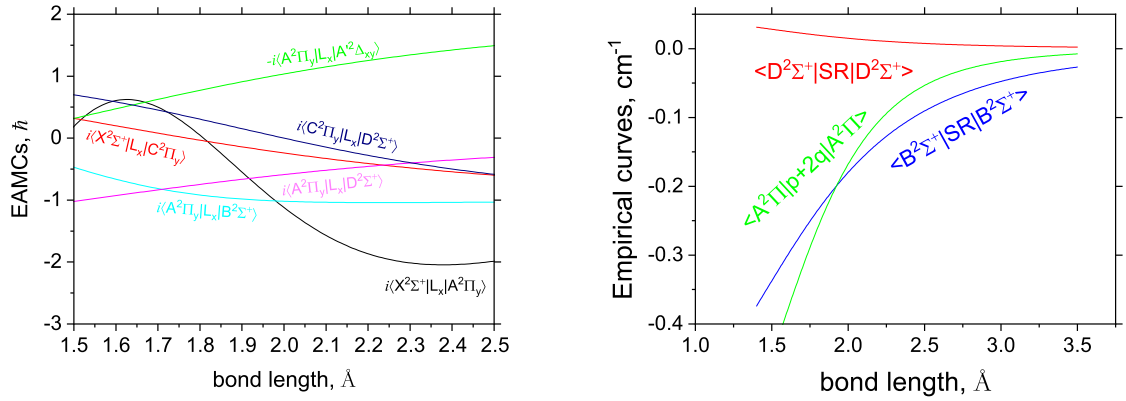

Figure 5. Refined EAMCs of YO in the diabatic representation, empirical spin–rotation corrections, and Λ-doubling curves.

to be doubly occupied. Augmented triple-zeta quality basis sets aug-cc-pwCVTZ (Peterson & Dunning 2002) on O and pseudo-potential-based aug-cc-pwCVTZ-PP (Peterson et al. 2007) on Y were used in these calculations. The resulting NACs are illustrated in Fig. 3.

5 SPECTROSCOPIC MODEL

Our starting point is the *ab initio* spectroscopic model of YO developed by Smirnov et al. (2019), which includes PECs, SOCs, TDMCs, EAMCs for six lowest doublet states of YO in the adiabatic representation. YO exhibits non-adiabatic effects via the couplings of the two pairs of states: $A\,^2\Pi$ with $C\,^2\Pi$ and $B\,^2\Sigma^+$ with $D\,^2\Sigma^+$. Apart from the avoided crossing in these PECs, other adiabatic curves (SOCs, EAMCs, and (T)DMCs) also have strongly distorted shapes exhibiting step-like behaviour, which makes the adiabatic representation far from ideal for refinement. This is not only because these curves are difficult to represent analytically as parametrized functions of the bond length (required for the fit), but also because the shapes of the curves around any avoided crossing are very sensitive to the precise position of these crossings, which are also difficult to control in the adiabatic representation. Due to these effects, SOCs, EAMCs, and (T)DMCs between the $B\,^2\Sigma^+$, $D\,^2\Sigma^+$ and the $A\,^2\Pi$, $C\,^2\Pi$ states also exhibit discontinuous behaviour in the region of the avoided crossing, which can only be correctly treated in combination with the NAC curves as well as their second-order derivative couplings (which we did not compute). Vibronic intensities, for instance, are very sensitive to the description of the steep structures in the adiabatic DMCs. Because of inaccuracies in the *ab initio* calculations, the adiabatic DMCs will be prone to large errors in their shape since the strong, steep gradient variations around the avoided crossing are sensitive to both crossing position and morphology, and so will negatively affect the corresponding spectral properties. These sharp behaviours are difficult to model, so the diabatic representation is a natural choice since DMCs and other couplings will become smooth, and less sensitive to inaccuracies in *ab initio* calculations.

We therefore decided to work in the diabatic representation taking advantage of the recent developments in DUO (Brady et al. 2022, 2023). To this end, a diabatic spectroscopic model of YO was generated by diabatizing the *ab initio* adiabatic PECs, SOCs, EAMCs, and (T)DMCs of YO (Smirnov et al. 2019) as outlined in the following.

Unfortunately, the *ab initio* adiabatic curves reported in Smirnov et al. (2019) were not suitable for a direct diabatization using the corresponding NACs due to incomplete *ab initio* curves and inconsistent levels of theory used for different properties. Effectively, only the PECs of the six electronic states of YO computed using the complete basis set limit (CBS) extrapolation from awCVQZ and awCV5Z in conjunction with the CCSD(T) method were suitable for accurate descriptions of the corresponding crossings in the diabatic representations. All other property curves (SOCs, EAMCs, and (T)DMCs) were computed with MRCI or even CASSCF and did not provide adequate coverage, especially at longer bond lengths ($r > 1.9$ Å) beyond the avoided crossing points (see figs 9 and 10 in Smirnov et al. 2019).

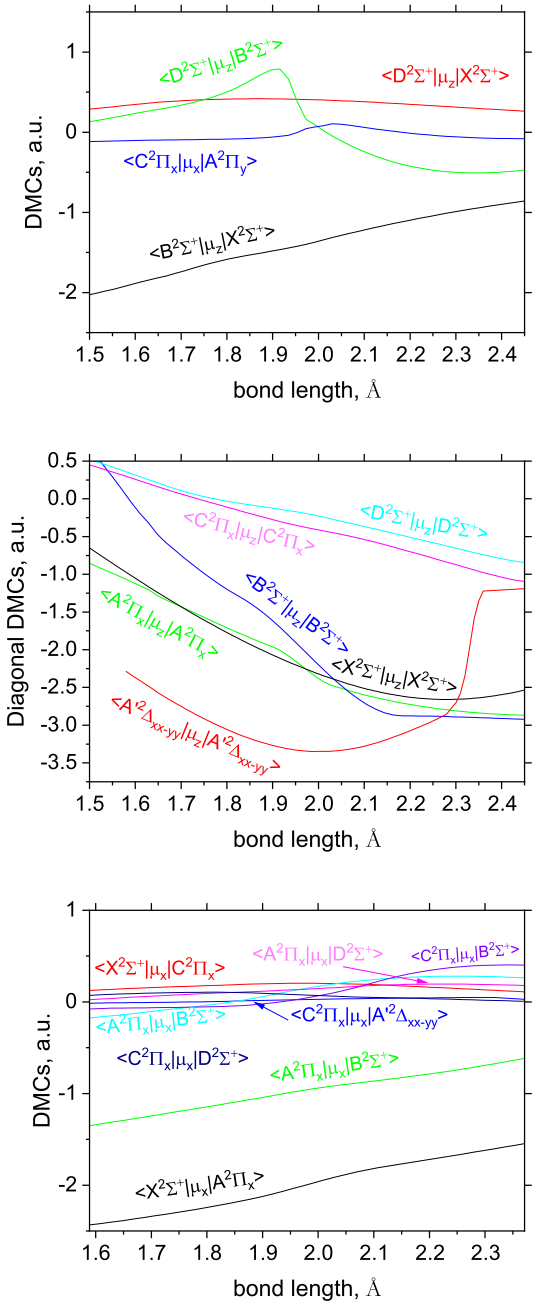

Figure 6. Diabatized *ab initio* dipole moment matrix elements (in au) as a function of bond length. The middle panel gives diagonal dipoles while the top and bottom panels give transition dipole moments.

In order to overcome this problem, in line with the property-based diabatization (see e.g. Shu et al. 2022), we constructed diabatic curves under the assumption that in the diabatic representations all the curves become smooth, without characteristic step-like shapes and manually constructed diabatic SOCs, EMACs, and TDMCs. The existing points were inter- and extrapolated to best represent smooth diabatic curves. Admittedly, there is some arbitrariness in this approach which is subsequently resolved, at least partially, by empirically refining the initial curves. The various curves representing our diabatic spectroscopic model of YO are illustrated in Figs 4–6.

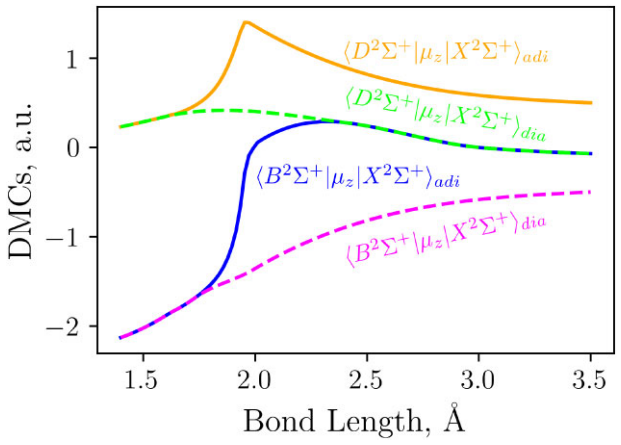

Figure 7. Example of the diabatization (see the text for details) of the adiabatic $\langle B\,^2\Sigma^+|\mu_z|X\,^2\Sigma^+\rangle$ and $\langle D\,^2\Sigma^+|\mu_z|X\,^2\Sigma^+\rangle$ dipole moment pairs, where the $B\,^2\Sigma^+$ and $D\,^2\Sigma^+$ states exhibit an avoided crossing at $r \sim 1.81$ Å.

5.1 Diabatization

To represent the diabatic PECs of the $X\,^2\Sigma^+$, $A\,^2\Pi$, $A'\,^2\Delta$, $B\,^2\Sigma^+$, $C\,^2\Pi$, and $D\,^2\Sigma^+$ states analytically, we used the extended Morse oscillator (EMO, Lee et al. 1999) function as well as the extended Hulburt–Hirschfelder (EHH) function (Hulburt & Hirschfelder 1941) as implemented in DUO. An EMO function is given by

$$V(r) = V_e + (A_e - V_e)\left[1 - \exp\left(-\sum_{k=0}^{N} B_k \xi_p^k (r - r_e)\right)\right]^2, \quad (2)$$

where A_e is a dissociation asymptote, $A_e - V_e$ is the dissociation energy, r_e is an equilibrium distance of the PEC, and ξ_p is the Šurkus variable given by:

$$\xi_p = \frac{r^p - r_e^p}{r^p + r_e^p}. \quad (3)$$

The EMO form is our typical choice for representing PECs and was used here for the $X\,^2\Sigma^+$, $A\,^2\Pi$, $B\,^2\Sigma^+$, and $D\,^2\Sigma^+$ states. For the $A'\,^2\Delta$ and $C\,^2\Pi$ states, which do not have much experimental information for refinement, we employ the EHH function. This form was suggested to be more suitable for the description of the dissociation region (Cazzoli, Cludi & Puzzarini 2006). Here, we use the EHH form from Ushakov et al. (2023) as given by

$$V_{\rm EHH}(r) = D_e\left[\left(1 - e^{-q}\right)^2 + cq^3\left(1 + \sum_{i=1}^{3} b_i q^i\right)e^{-2q}\right], \quad (4)$$

where $q = \alpha(r - r_e)$.

The corresponding parameters defining PECs were first obtained by fitting to the *ab initio* CCSD(T)/CBS potential energies and then empirically refined by fitting to empirical energies of YO (where available) as described below; these parameters are given in the Supporting Information in the form of a DUO input file. The asymptotic energies A_e for all states but $B\,^2\Sigma^+$ were fixed to the value 59220 cm^{-1}, or 7.34 eV, which corresponds to $D_0 = 7.290(87)$ eV determined by Ackermann & Rauh (1974), based on their mass spectrometric measurements. For the $B\,^2\Sigma^+$ state, A_e was fixed to a higher value of 75000 cm^{-1} in order to achieve a physically sensible shape of the PEC. Otherwise, the $B\,^2\Sigma^+$ curve tended to cross the $D\,^2\Sigma^+$ curve also at $r \sim 4$ Å.

In principle, the property-based diabatization does not require the usage of the NAC curves. However, in order to assist our diabatizations of the YO *ab initio* curves, we used the *ab initio*

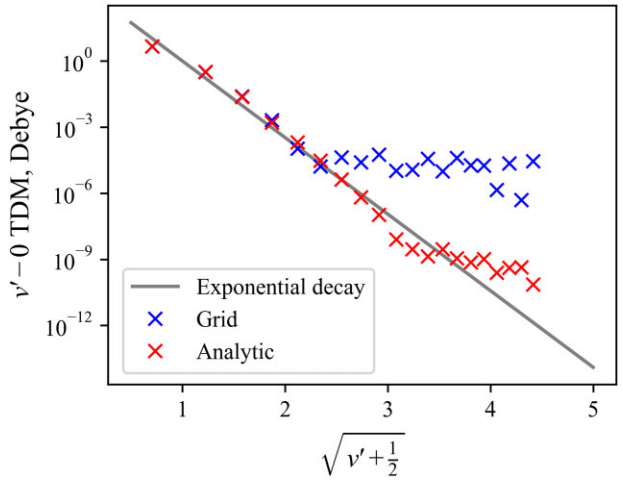

Figure 8. $X\,^2\Sigma^+ \rightarrow X\,^2\Sigma^+$ $\nu'-0$ overtone TDMs are plotted on a log scale versus $\sqrt{\nu'+\frac{1}{2}}$ and are computed using the grid interpolated *ab initio* DMC (shown as blue circles) and our fitted analytical model DMC (equation 15, shown as red crosses). A simple exponential decay is shown for comparison which simulates the expected NIDL-like behaviour (Medvedev 2012).

CASSCF NACs of *A*–*C* and *B*– *D* shown in Fig. 3 as a guide. These curves were fitted using the following Lorentzian functions:

$$\phi_{ij}(r) = \frac{1}{2}\frac{\gamma}{\gamma^2 + (r - r_c)^2}, \tag{5}$$

where γ is the corresponding half width at half-maximum (HWHM), while r_c is its centre, corresponding to the crossing point of diabatic curves.

The diabatic and adiabatic representations are connected via a unitary 2×2 transformation given by

$$\mathbf{U}(\beta(r)) = \begin{bmatrix} \cos(\beta(r)) & -\sin(\beta(r)) \\ \sin(\beta(r)) & \cos(\beta(r)) \end{bmatrix}, \tag{6}$$

where the r-dependent mixing angle $\beta(r)$ is obtained via the integral

$$\beta(r) = \int_{-\infty}^{r} \phi_{12}(r')\mathrm{d}r'. \tag{7}$$

For the Lorentzian-type NAC in equation (5), the angle β is given by

$$\beta = \frac{1}{2}\arctan\left(\frac{r - r_c}{\gamma}\right) + \frac{\pi}{4}. \tag{8}$$

The diabatic representation is defined by two PECs $V_1(r)$ and $V_2(r)$ coupled with a diabatic term $D(r)$ as a 2×2 diabatic matrix

$$\mathbf{A} = \begin{pmatrix} V_1(r) & D(r) \\ D(r) & V_2(r) \end{pmatrix}. \tag{9}$$

The two eigenvalues of the matrix **A** provide the adiabatic PECs in the form of solution of a quadratic equation as given by

$$V_{\rm low}(r) = \frac{V_1(r) + V_2(r)}{2} - \frac{\sqrt{[V_1(r) - V_2(r)]^2 + 4\,D^2(r)}}{2}, \tag{10}$$

$$V_{\rm upp}(r) = \frac{V_1(r) + V_2(r)}{2} + \frac{\sqrt{[V_1(r) - V_2(r)]^2 + 4\,D^2(r)}}{2}, \tag{11}$$

where $V_{\rm low}(r)$ and $V_{\rm upp}(r)$ are the two adiabatic PECs.

Assuming the diabatic PECs $V_1(r)$ and $V_2(r)$ as well as NAC $\phi_{12}(r)$ are known, the diabatic coupling function $D(r)$ can be reconstructed using the condition that the non-diagonal coupling should vanish upon the unitary transformation $U(r)$ in equation (6) such that the adiabatic potential matrix is diagonal and is then given by:

$$D(r) = \frac{1}{2}\tan(2\beta(r))\,(V_2(r) - V_1(r)). \tag{12}$$

Assuming also the EMO functions for the PECs $V_1(r)$ and $V_2(r)$ as in equation (2) and the 'Lorentzian'-type angle $\beta(r)$ in equation (8), the diabatic coupling curves for YO have an asymmetric Gaussian-like shape, see the right panel of Fig. 3; this is not always the case as the $V_2 - V_1$ term in equation (12) heavily influences the morphology of $D(r)$.

For the $B\,^2\Sigma^+$–$D\,^2\Sigma^+$ pair, where the experimental data are better represented, in order to introduce some flexibility into the fit, we decided to model the diabatic coupling by directly representing it using an inverted EMO function from equation (2). This gives the asymmetric Gaussian-like shape, with the asymptote A_e set to zero and V_e representing the maximum of the diabatic coupling $D(r)$. The *A*–*C* diabatic coupling was modelled using equation (12) with the two parameter 'Lorentzian'-type angle $\beta(r)$ from equation (8).

5.2 Other coupling curves

For the SOC and EAMC curves of YO, we used the expansion:

$$F(r) = \sum_{k=0}^{N} B_k\, z^k (1 - \xi_p) + \xi_p\, B_\infty, \tag{13}$$

where z is either taken as the Šurkus variable $z = \xi_p$ or a damped-coordinate given by:

$$z = (r - r_{\rm ref})\, e^{-\beta_2 (r - r_{\rm ref})^2 - \beta_4 (r - r_{\rm ref})^4}, \tag{14}$$

see also Prajapat et al. (2017) and Yurchenko et al. (2018a). Here, $r_{\rm ref}$ is a reference position equal to r_e by default and β_2 and β_4 are damping factors. For the $X\,^2\Sigma^+$ state, a BOB (Born–Oppenheimer Breakdown) correction curve modelled using equation (13) was used. These parametrized representations were then used to refine the *ab initio* curves by fitting them to the experimentally derived rovibronic energies of YO. The final coupling curves are shown in Figs 3 (right display), 4, and 5.

We also included spin-rotation and Λ-doubling $p(r) + 2o(r)$ (Brown & Merer 1979) curves as empirical objects for some of the electronic states modelled using equation (13), see Fig. 5.

5.3 Dipoles

We diabatize our DMCs using a combination of cubic-spline interpolation to smooth out the region around the avoided crossing and knowledge of the shape of the diabatized target curves. Fig. 7 illustrates our property-based diabatizing 'transformation' for the $\langle B\,^2\Sigma^+|\mu_z|X\,^2\Sigma^+\rangle$ and $\langle D\,^2\Sigma^+|\mu_z|X\,^2\Sigma^+\rangle$ transition dipole moment pairs, the effect being the two curves 'swap' beyond the avoided crossing and are now smooth. Fig. 6 shows all diabatized *ab initio* diagonal and off-diagonal DMCs, which are smooth over all bond lengths.

Within nuclear-motion and intensity calculations dipoles are sometimes represented as a grid of *ab initio* points, however, one sees a flattening of the ground-state IR overtone bands with vibrational excitation. The source of this non-physical flattening has been discussed by Medvedev et al. (2015, 2016), Medvedev & Ushakov (2022), and Ushakov et al. (2023). It comes from numerical noise in

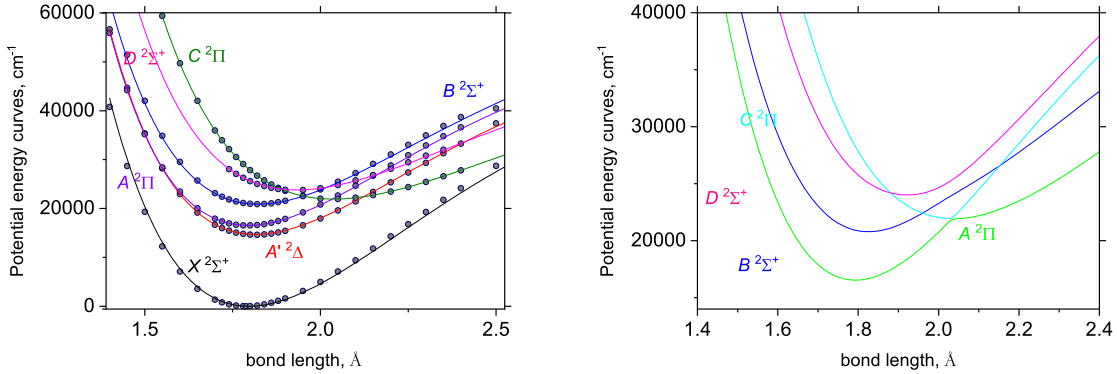

Figure 9. Refined (lines) and *ab initio* (points) PECs of YO: diabatic (left) and adiabatic (right).

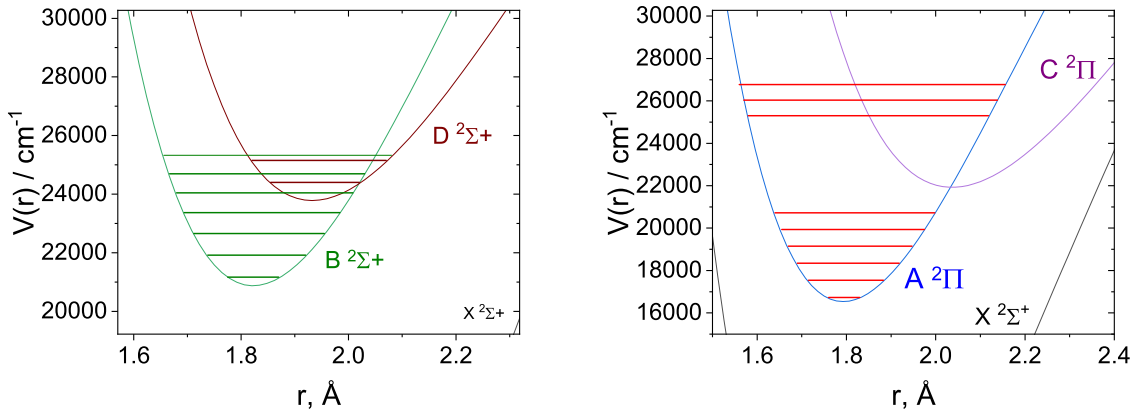

Figure 10. Diabatic PECs of the *B*/*D* and *A*/*C* pairs with the corresponding experimental energy term values ($J = 0.5$).

the calculations, which is enhanced by the interpolation of the given MOLPRO dipole grid points onto the DUO defined grid. The most effective method to reduce this numerical noise is to represent the input dipole moments analytically (Medvedev et al. 2015). We chose to represent our $X\,^2\Sigma^+$ DMC using the 'irregular DMC' proposed by Medvedev & Ushakov (2022) which takes the form

$$\mu_{\rm irreg}(r) = \chi(r; c_2, ..., c_6) \sum_{i=0}^{6} b_i T_i(z(r)), \tag{15}$$

where T_i are Chebyshev polynomials of the first kind, b_i are summation coefficients to be fitted, $z(r)$ is a reduced variable in bond length, and is given by

$$z(r) = 1 - 2e^{-c_1 r}, \tag{16}$$

which maps the $r \in [0, \infty]$ Å interval to the $z \in [-1, 1]$ reduced interval (the region in which the Chebyshev polynomials have zeros), and finally $\chi(r; c_2, \ldots, c_6)$ is an r-dependent term parametrically dependent on 5 c_k parameters to be fitted and is given by

$$\chi(r; c_2, ..., c_6) \frac{(1 - e^{-c_2 r})^3}{\sqrt{(r^2 - c_3^2)^2 + c_4^2}\sqrt{(r^2 - c_5^2)^2 + c_6^2}}.$$

The irregular DMC form has the desirable properties of quickly converging to the correct long-range limit, having enough parameters (13) to ensure minimal local oscillations, and provide a straight normal intensity distribution law (NIDL, Medvedev & Ushakov 2022; Medvedev 2012; Medvedev et al. 2015). This straight NIDL is a major restriction to the model DMC and means the logarithm of the overtone vibrational transition dipole moments (VTDM) $\langle v'|\mu(r)|v = 0\rangle$ ($v' > 1$) should evolve linearly with the square root of the upper state energy over the harmonic frequency, or $\sqrt{v' + \frac{1}{2}}$. Here, we compute VTDMs $\langle v'|\mu(r)|v = 0\rangle$ up to dissociation for the $X\,^2\Sigma^+$ using both the grid-defined dipole and the fitted analytical form, where Fig. 8 shows their behaviour. The expected linear behaviour of the NIDL is shown in Fig. 8 as a grey line which is seen to better agree with the TDM computed using the analytical $X\,^2\Sigma^+$ DMC compared to the calculation using the grid-interpolated DMC. At the $v' = 6$ overtone the grid-interpolated DMC causes a non-physical flattening of the VTDM at $\sim 3.4 \times 10^{-5}$ D (Debye), whereas we only see a departure from the straight NIDL at $v' = 15$ when using the analytical form which flattens at $\sim 7.4 \times 10^{-10}$ D. The analytically represented $X\,^2\Sigma^+$ DMC therefore provides a more physically meaningful behaviour of the vibrational overtone VTDM but still departs from the expected NIDL at high overtones where the intensities are much lower and therefore less important.

Following Smirnov et al. (2019), we scaled the *ab initio* DMC of $X\,^2\Sigma^+$ by the factor 1.025 to match the experimental value of the equilibrium dipole $\langle X|, v = 0|\mu(r)|X, v = 0\rangle$ determined by Suenram et al. (1990). The DMCs of $A'\,^2\Delta$, $A\,^2\Pi$, and $B\,^2\Sigma^+$ were scaled by 0.97, 0.86 and 0.6, respectively to match the more accurate CCSD(T)/CBS single point calculations from Smirnov et al. (2019).

The $A\,^2\Pi$–$X\,^2\Sigma^+$, $B\,^2\Sigma^+$–$X\,^2\Sigma^+$, and $D\,^2\Sigma^+$–$X\,^2\Sigma^+$ TDMCs had to be scaled by 0.8, 0.75, and 2.8, respectively, to improve the agreement of the corresponding calculated values of the $A\,^2\Pi$,

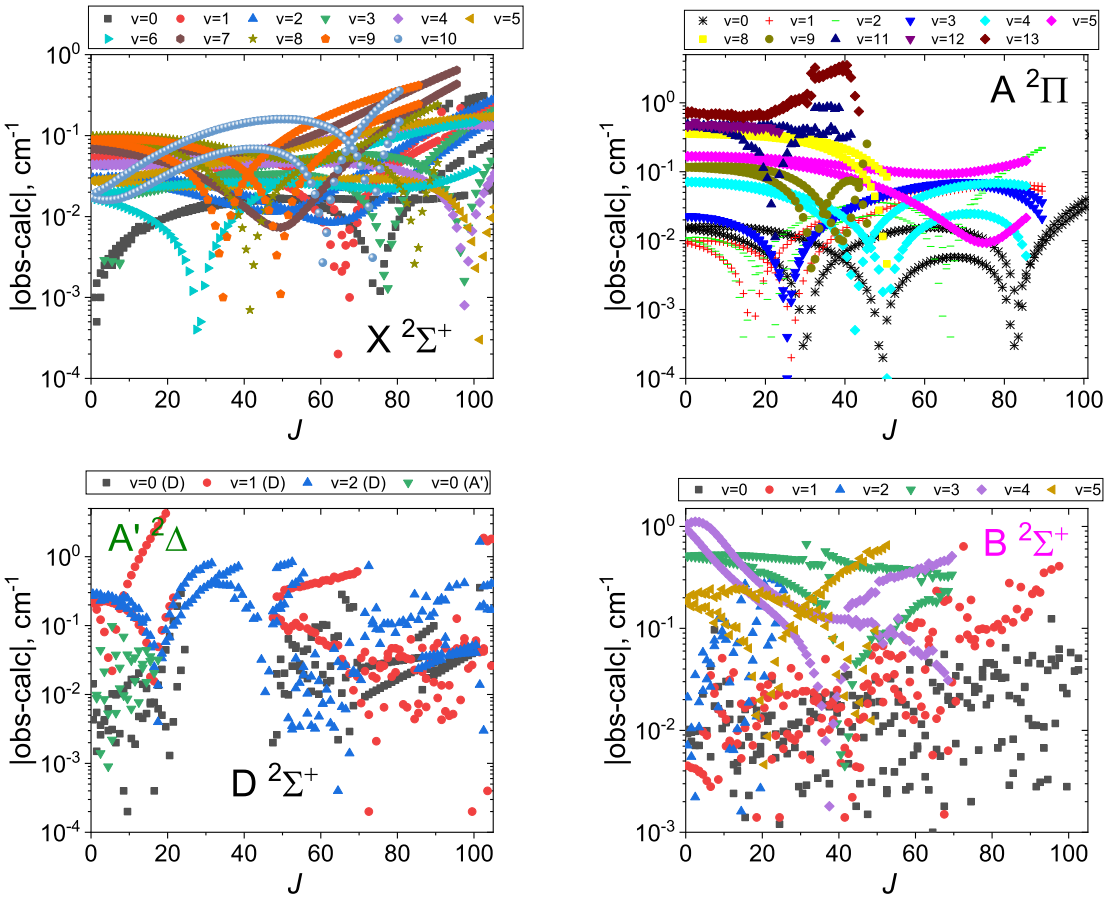

Figure 11. Observed minus calculated residuals for YO using the refined spectroscopic model for different vibronic states.

Table 1. Extract from the states file of the line list for YO.

i	Energy (cm^{-1})	g_i	J	unc	τ	g	Parity	State	v	Λ	Σ	Ω	Ma/Ca	Energy (cm^{-1})
329	17109.384230	8	1.5	0.060200	0.000000	−0.000268	+ f	A2Pi	1	1	−0.5	0.5	Ma	17109.393106
330	17486.768827	8	1.5	0.220200	0.002928	−0.400448	+ f	X2Sigma +	22	0	0.5	0.5	Ca	17486.768827
331	17538.074400	8	1.5	0.060200	0.000000	0.798897	+ f	A2Pi	1	1	0.5	1.5	Ma	17538.062594
332	17635.333239	8	1.5	4.030000	0.000757	0.399545	+ f	Ap2Delta	4	2	−0.5	1.5	Ca	17635.333239
333	17916.112120	8	1.5	0.110200	0.000000	−0.000268	+ f	A2Pi	2	1	−0.5	0.5	Ma	17916.122345
334	18210.832409	8	1.5	0.230200	0.002827	−0.400448	+ f	X2Sigma +	23	0	0.5	0.5	Ca	18210.832409
335	18345.385550	8	1.5	0.110200	0.000000	0.798904	+ f	A2Pi	2	1	0.5	1.5	Ma	18345.398884
336	18403.241526	8	1.5	5.030000	0.000554	0.399553	+ f	Ap2Delta	5	2	−0.5	1.5	Ca	18403.241526

Notes. i: state counting number.
$\tilde{E}$: state energy term values in cm^{-1}, MARVEL or Calculated (DUO).
g_i: total statistical weight, equal to $g_{ns}(2J + 1)$.
J: total angular momentum.
unc: uncertainty (cm^{-1}).
τ: lifetime (s^{-1}).
g: Landé g-factors (Semenov, Yurchenko & Tennyson 2016).
+/ −: total parity.
e/f: rotationless parity.
State: electronic state.
v: state vibrational quantum number.
Λ: projection of the electronic angular momentum.
Σ: projection of the electronic spin.
Ω: projection of the total angular momentum, $\Omega = \Lambda + \Sigma$.
Label: 'Ma' is for MARVEL and 'Ca' is for Calculated.
Energy: state energy term values in cm^{-1}, Calculated (DUO).

Table 2. Extract from the transitions file of the line list for YO.

f	i	A_{fi} (s^{-1})	$\tilde{\nu}_{fi}$
78884	78556	4.1238E+02	10000.000225
111986	112128	6.0427E+01	10000.000489
69517	69133	5.2158E−03	10000.000708
39812	40514	7.3060E−02	10000.000818
34753	33815	6.2941E−04	10000.001400
72754	72910	2.5370E+00	10000.001707
130747	130937	5.3843E−04	10000.002153
130428	130122	1.5407E−02	10000.002287
114934	115604	3.2160E+00	10000.002360
12357	11958	6.2849E+02	10000.002755
135752	135933	1.4867E+01	10000.004338

Notes. f: upper state counting number.
i: lower state counting number.
A_{fi}: Einstein-A coefficient in s^{-1}.
$\tilde{\nu}_{fi}$: transition wavenumber in cm^{-1}.

Table 3. Parameters used to estimate uncertainties of the YO calculated energy term values according to equation (17).

State	ΔT	$\Delta\omega$	ΔB
$X\,^2\Sigma^+$	0.0	0.01	0.0001
$A\,^2\Pi$	0.01	0.05	0.0001
$C\,^2\Pi$	10.0	1.0	0.01
$B\,^2\Sigma^+$	0.01	0.057	0.0001
$D\,^2\Sigma^+$	0.01	0.07	0.0001
$A'\,^2\Delta$	0.01	1	0.01

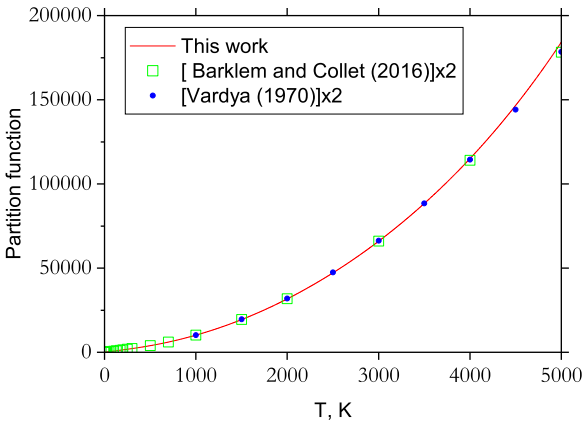

Figure 12. Partition functions of YO: from this work (solid line), from Vardya (1970, filled circles) and from Barklem & Collet (2016, open squares). The latter two were multiplied by a factor of 2 to account for the different treatment of nuclear statistics.

$B\,^2\Sigma^+$, and $D\,^2\Sigma^+$ lifetimes with the measurements of Liu & Parson (1977) and Zhang et al. (2017), see Table 4 and discussion below.

6 REFINEMENT OF THE SPECTROSCOPIC MODEL

We use the diatomic code DUO (Yurchenko et al. 2016) to solve a coupled system of Schrödinger equations. DUO is a free-access rovibronic solver for diatomic molecules available at https://github.com/exomol/Duo/. The hyperfine structure was ignored. For nuclear-motion calculations a vibrational sinc-DVR basis set was defined

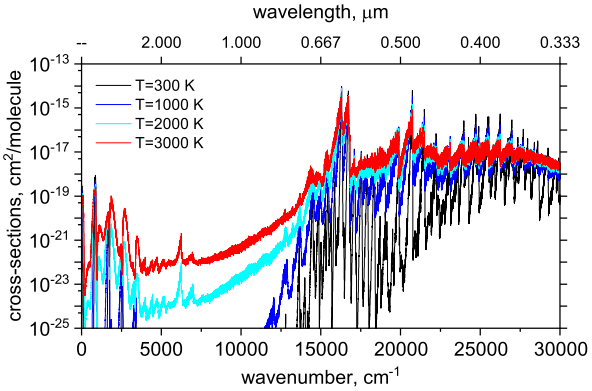

Figure 13. The simulated YO absorption spectrum computed at different temperatures. We adopt a Lorentzian line broadening of 1 cm^{-1} for each line which is computed at a resolution of 1 cm^{-1}. We see the intensity deviation is greatest around 0.5 and 0.6 μm where the $X\,^2\Sigma^+ \rightarrow A\,^2\Pi$ and $X\,^2\Sigma^+ \rightarrow B\,^2\Sigma^+$ bands dominate opacity.

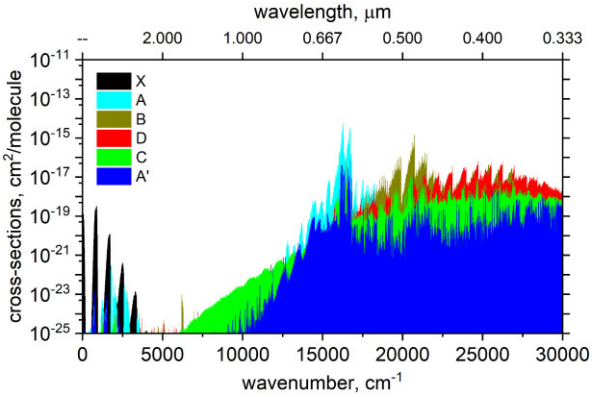

Figure 14. Different electronic band components of the absorption spectrum simulated at 2000 K using Lorentzian line broadening of 1 cm^{-1} for each line computed at a resolution of 1 cm^{-1}.

Table 4. Lifetimes of $^{89}Y^{16}O$ states in ns: comparison with the measurements of [77LiPa] (Liu & Parson 1977) and [17ZhZhZh] (Zhang et al. 2017), and the *ab initio* calculations of [19SmSoYu] (Smirnov et al. 2019).

State	v	[77LiPa]	[17ZhZhZh]	[19SmSoYu]	This work
$A\,^2\Pi_{1/2}$	0	33.0 ± 1.3		22.6	35.5
	1	36.5 ± 2.4		23.0	36.1
$A\,^2\Pi_{3/2}$	0	32.3 ± 0.9		20.9	32.7
	1	30.4 ± 1.8		21.3	33.3
	2	33.4 ± 1.5		21.6	33.9
	6	41.6 ± 2.1		29.2	37.3
$B\,^2\Sigma^+$	0	30.0 ± 0.9	38 ± 5	32.5	30.7
	1	32.5 ± 1.2		34.3	30.4
$D\,^2\Sigma^+$	0		79 ± 5	30.1	62.5
	1		79 ± 5	29.2	56.8

as a grid of 151 internuclear geometries in the range of 1.4–3.5 Å. We select the lowest 30, 30, 35, 30, 30, and 30 vibrational wavefunctions of the $X\,^2\Sigma^+$, $A'\,^2\Delta$, $A\,^2\Pi$, $B\,^2\Sigma^+$, $C\,^2\Pi$, and $D\,^2\Sigma^+$ states, respectively, to form the contracted vibronic basis. A refined spectroscopic model of YO was obtained by fitting the expansion parameters representing different properties to 5089

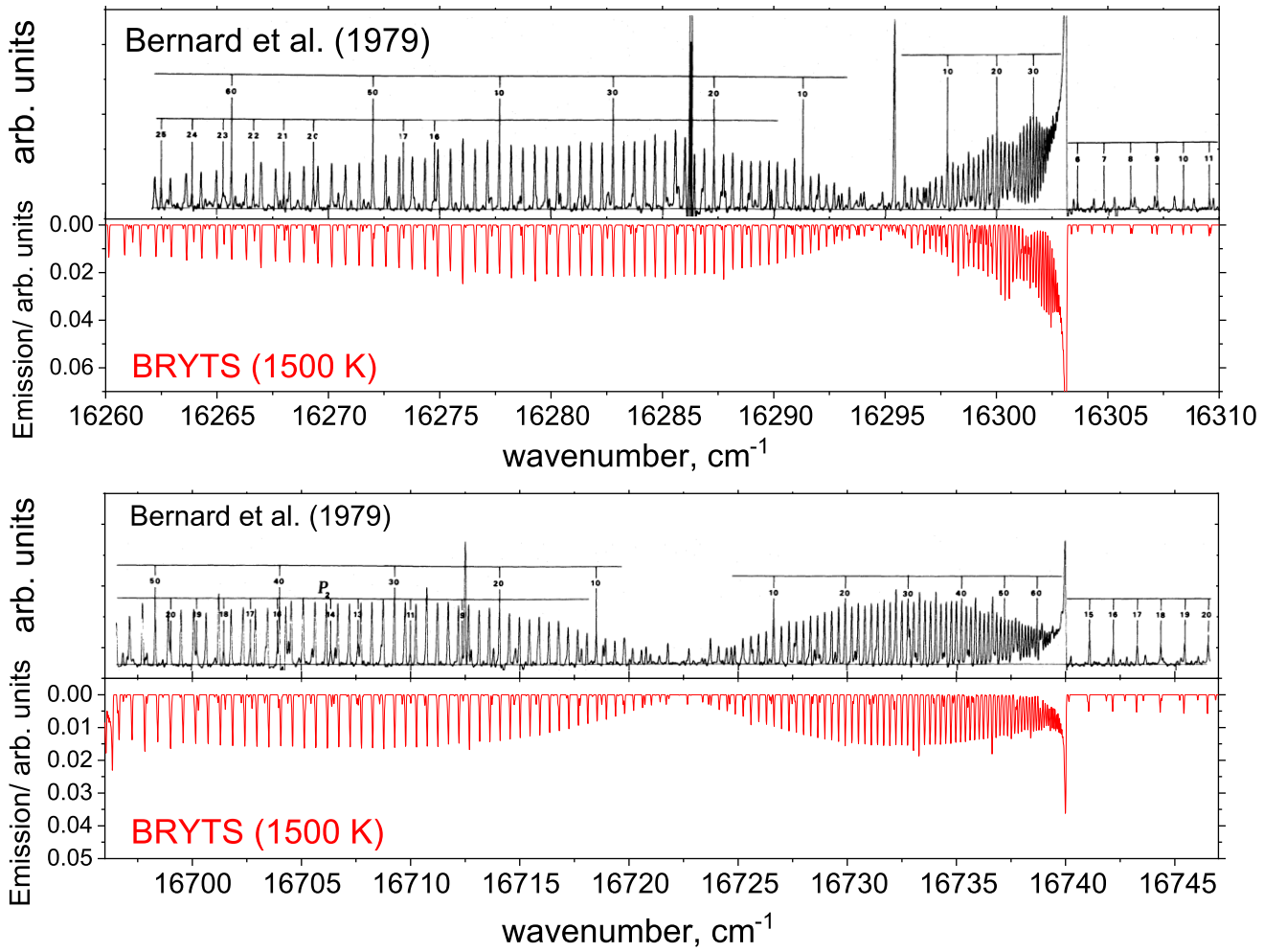

Figure 15. Comparison of our computed $A\,^2\Pi_{1/2} \rightarrow X\,^2\Sigma^+$ and $A\,^2\Pi_{3/2} \rightarrow X\,^2\Sigma^+$ rotational-electronic emission bands (lower displays) with those of Bernard, Bacis & Luc (1979), a measured spectrum using Fourier transform spectroscopy (upper displays). We compute our spectrum at a temperature of 1500 K to best match that of Bernard, Bacis & Luc (1979). A Gaussian line profile of 0.065 cm^{-1} was used with a resolution of 0.01 cm^{-1}. © AAS. Reproduced with permission.

empirically derived rovibrational energy term values of $^{89}Y^{16}O$ described above.

The refined (diabatic) PECs of YO are illustrated in Fig. 9. The CCSD(T)/CBS *ab initio* energies from Smirnov et al. (2019), shown with circles, appear to closely follow the refined curves, indicating the excellent quality of the *ab initio* CCSD(T) PECs.

Diabatic representations of the $A\,^2\Pi$, $B\,^2\Sigma^+$, $C\,^2\Pi$, and $D\,^2\Sigma^+$ states are illustrated in Fig. 10, where the corresponding experimental energy term values are also shown ($J = 0.5$ or 1.5). Due to the very close positioning of the $D\,^2\Sigma^+$ ($v = 2$) and $B\,^2\Sigma^+$ ($v = 6$) states, the $B\,^2\Sigma^+$ ($v = 6$) rovibronic wavefunctions appear strongly mixed with the $D\,^2\Sigma^+$ ($v = 2$) wavefunctions in the DUO solution, especially at higher J.

The $B\,^2\Sigma^+$ vibronic energies of $v \geq 4$ are strongly affected by the diabatic coupling with the $D\,^2\Sigma^+$ state. Introduction of the diabatic coupling to the $B\,^2\Sigma^+$ states makes the shape of the PEC broader and pushes the positions of the $B\,^2\Sigma^+$ energies down. It is interesting to note that the $A\,^2\Pi$ state vibronic energies for $v = 11$, 12, and 13 do not appear to be very perturbed by the presence of the close-by $C\,^2\Pi$ state, unlike the interaction of the *B*/*D* diabatic pair. This can be attributed to the difference in the corresponding NACs of the *B*/*D* and *A*/*C* pairs in Fig. 3.

By construction, all DUO eigenfunctions and eigenvalues are automatically assigned the rigorous quantum numbers J and parity $\tau = \pm 1$. To assign the non-rigorous rovibronic quantum numbers, DUO first defines the spin-electronic components ('State' and Ω) using the largest contribution from the eigencoefficients approach (Yurchenko et al. 2016). Within each rotation-spin-electronic state, the vibrational excitation is then defined by a simple count of the increasing energies starting from $v = 0$.

The refined SOCs, EAMCs, and TDMCs of YO are shown in Fig. 4. The refined diabatic couplings for the *B*–*D* and *A*–*C* pairs are shown in Fig. 3.

All parameters defining the final spectroscopic model of YO are included in the Supporting Information as a DUO input file.

The results of the fittings are illustrated in Fig. 11, where |obs.-calc.| residuals are shown for different electronic states. Some of the bands show clear systematic behaviour of the residuals with respect to J, especially those that correspond to the synthetic data or high resolution data (e.g. $X\,^2\Sigma^+$, $A\,^2\Pi$ and some of the $B\,^2\Sigma^+$

Table 5. Comparison of the experimental (Bernard & Gravina 1983) and theoretical (this work) positions of the band heads in the $A\,^2\Pi$–$X\,^2\Sigma^+$ system.

v'	v''	Branch	$J_{\rm head}$ (obs)	$J_{\rm head}$ (calc)	$\tilde{\nu}_{\rm exp}$	$\tilde{\nu}_{\rm calc}$	$\Delta\tilde{\nu}$
0	1	Q_1	93.5	98.5	15456.10	15456.61	−0.51
1	2	Q_1	87.5	88.5	15417.24	15417.45	−0.21
2	3	Q_1	77.5	79.5	15377.56	15377.77	−0.21
3	4	Q_1	70.5	71.5	15337.30	15337.45	−0.15
4	5	Q_1	62.5	63.5	15296.26	15296.37	−0.11
5	6	Q_1	56.5	56.5	15254.24	15254.41	−0.17
6	7	Q_1	49.5	50.5	15210.78	15211.28	−0.50
8	9	Q_1	37.5	39.5	15123.48	15123.34	0.14
9	10	Q_1	33.5	35.5	15077.15	15077.28	−0.13
10	11	Q_1		27.5	15033.33	15030.30	3.03
11	12	Q_1		25.5	14981.00	14981.17	−0.17
12	13	Q_1		26.5	14933.83	14934.60	−0.77
13	14	Q_1		23.5	14880.28	14882.94	−2.66
14	15	Q_1		19.5	14829.85	14832.44	−2.59
15	16	Q_1		18.5	14774.01	14778.50	−4.49
16	17	Q_1		18.5	14718.59	14725.27	−6.68
17	18	Q_1		17.5	14654.49	14671.33	−16.84
18	19	Q_1		16.5	14615.68	14616.53	−0.85
20	21	Q_1		63.5	14535.74	14541.80	−6.06
21	22	Q_1		59.5	14494.52	14479.62	14.90
22	23	Q_1		54.5	14452.30	14416.66	35.64
0	0	Q_1	51.5	51.5	16303.10	16303.16	−0.06
0	0	R_2	79.5	81.5	16739.90	16740.01	−0.11
1	1	Q_1	47.5	48.5	16259.93	16259.89	0.04
1	1	R_2	72.5	74.5	16696.30	16696.36	−0.06
2	2	Q_1	44.5	44.5	16215.91	16215.89	0.02
2	2	R_2	66.5	68.5	16652.15	16652.10	0.05
3	3	Q_1	40.5	41.5	16171.00	16171.02	−0.02
3	3	R_2	61.5	62.5	16607.07	16607.07	0.00
4	4	Q_1	37.5	37.5	16125.08	16125.20	−0.12
4	4	R_2	56.5	57.5	16561.11	16561.16	−0.05
5	5	Q_1	34.5	35.5	16078.10	16078.30	−0.20
5	5	R_2	51.5	52.5	16514.06	16514.08	−0.02
6	6	Q_1	31.5	32.5	16029.60	16030.15	−0.55
6	6	R_2		35.5	16462.40	16462.74	−0.34
7	7	R_2	43.5	44.5	16417.60	16418.85	−1.25
8	8	Q_1	26.5	27.5	15932.00	15931.69	0.31
8	8	R_2	37.5	37.5	16367.89	16370.33	−2.44
9	9	Q_1	24.5	25.5	15880.20	15880.17	0.03
9	9	R_2	33.5	35.5	16315.88	16317.95	−2.07
10	10	Q_1		22.5	15828.06	15827.76	0.30
11	11	Q_1		19.5	15773.23	15773.03	0.20
12	12	Q_1		20.5	15720.30	15720.47	−0.17

systems), while others appear random with no particular structure (e.g. $v = 0$ of $B\,^2\Sigma^+$ and $D\,^2\Sigma^+$). No other obvious trends could be seen.

The root-mean-squares error achieved is 0.29 cm^{-1} for all 5906 energies covering J up to 142.5.

There are no experimental data on the $C\,^2\Pi$ state due to its large displacement from the Franck–Condon region of the $X\,^2\Sigma^+$ state. We therefore had to rely on the available *ab initio* curves associated with this state as well as on their quality. Unlike the CCSD(T) PECs, the corresponding coupling curves were computed with MRCI and are less accurate. Moreover, there is no experimental data representing perturbations caused by the $C\,^2\Pi$ rovibronic state on other vibronic states in the limited experimental data on YO. However theoretically, using the *ab initio* data, we do see such perturbations in the $A\,^2\Pi$, $B\,^2\Sigma^+$, and $D\,^2\Sigma^+$ states due to the spin–orbit and EAM couplings with $C\,^2\Pi$ (see Smirnov et al. 2019), which makes the fit especially difficult. We therefore decided to switch-off all the coupling with the $C\,^2\Pi$ state in this work.

The experimental data on the $A'\,^2\Delta$ state are limited to $v = 0$ ($J \leq 17.5$), which means only the potential minimum $V_{\rm e}$ of the $A'\,^2\Delta$ state and the corresponding equilibrium constant could be usefully refined, but not its shape, which was fixed to the *ab initio* CCSD(T) curve via the corresponding EHH potential parameters.

7 LINE LIST

Using our final semi-empirical spectroscopic model, a rovibronic line list of ^{89}Y^{16}O called BRYTS covering the lowest six doublet electronic states and the wavelength range up to 166.67 nm was produced. In total 60 678 140 Einstein A coefficients between 173 621 bound rovibronic states were computed with a maximum total rotational quantum number $J_{\rm max} = 400.5$. ^{89}Y is the only stable

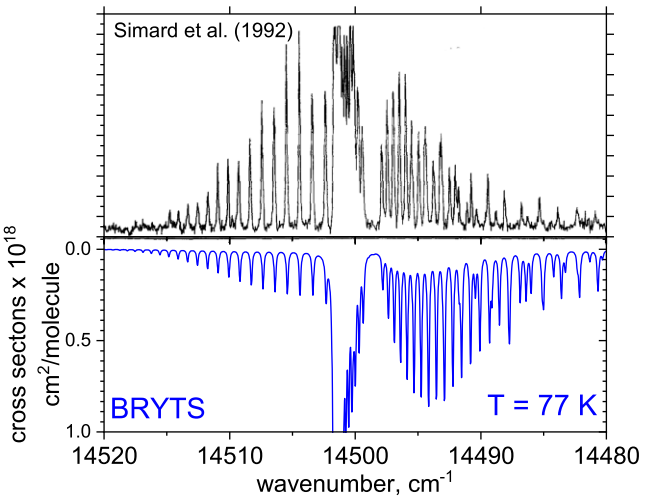

Figure 16. Comparison of the computed emission $A'\,^2\Delta - X\,^2\Sigma^+$ (0,0) band with the measurements of Simard et al. (1992) at $T = 77$ K and Lorentzian line profile of HWHM $= 0.04$ cm^{-1}.

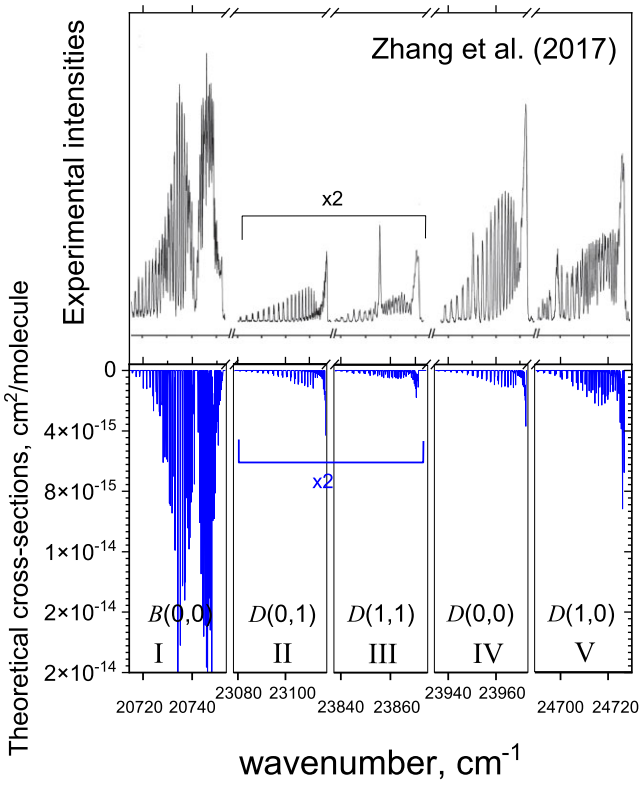

Figure 17. Comparison of our computed (bottom) $D\,^2\Sigma^+$–$X\,^2\Sigma^+$ absorption spectra to the measurements of Zhang et al. (2017, top). The simulations assumed a cold rotational temperature of $T_{\rm rot} = 50$ K and a hot vibrational temperature of $T_{\rm vib} = 800$ K. A Doppler line profile corresponding to $T_{\rm rot} = 50$ K was used.

isotope of yttrium; however, using the same model, line lists for two minor isotopologues ^{89}Y^{17}O and ^{89}Y^{18}O have been also generated.

The line lists are presented in the standard ExoMol format (Tennyson, Hill & Yurchenko 2013; Tennyson et al. 2020) consisting of a States file and a Transitions file with extracts shown in Tables 1 and 2, respectively. The calculated energies in the States file are 'MARVELized', that is, we replace them with the (pseudo-)MARVEL values where available. The uncertainties are taken as the experimental (pseudo-)MARVEL uncertainties for the substituted values, otherwise the following empirical and rather conservative expression is used:

$$\text{unc.} = \Delta T + \Delta\omega\, v + \Delta B\, J(J+1), \tag{17}$$

with the state-dependent parameters listed in Table 3.

The partition function of YO computed using the new line list is shown in Fig. 12, where it is compared to the partition functions by Barklem & Collet (2016) and Vardya (1970), showing close agreement once a correction is made for the fact that ^{89}Y has nuclear spin $\frac{1}{2}$. We also generate temperature- and pressure-dependent opacities of YO using the BRYTS line list and by following the ExoMolOP procedure (Chubb et al. 2021) for four exoplanet atmosphere retrieval codes ARCiS (Min et al. 2020), TauREx (Al-Refaie et al. 2021), NEMESIS (Irwin et al. 2008), and petitRADTRANS (Molliére et al. 2019).

The BRYTS line lists, partition function, and opacities are available at www.exomol.com.

8 SIMULATED SPECTRA

Using the computed line list for YO, here we simulate the YO rovibronic absorption spectra using the program ExoCross (Yurchenko, Al-Refaie & Tennyson 2018b). Fig. 13 shows the temperature variation of the YO rovibronic spectrum over the spectroscopic range up to 166 nm. Fig. 14 highlights the contribution of the most important electronic bands to the total opacity simulated at 2000 K such that there is good separation between the electronic bands. In both simulations, each line was broadened using a Lorentzian line profile with an HWHM of 1 cm^{-1} and computed at a resolution of 1 cm^{-1}.

8.1 Lifetimes

Table 4 compares our lifetimes to the experimental and theoretical values from the literature: laser fluorescence measurements of the $A\,^2\Pi$ and $B\,^2\Sigma^+$ states ($v \leq 2$) of YO by Liu & Parson (1977) and $B\,^2\Sigma^+$ ($v = 0$) and $D\,^2\Sigma^+$ ($v = 0, 1$) lifetimes by Zhang et al. (2017) as well as to the theoretical values by Langhoff & Bauschlicher (1988) and Smirnov et al. (2019). The theoretical values correspond to the lowest J values, $J = 0.5$ for $X\,^2\Sigma^+$, $B\,^2\Sigma^+$ and $D\,^2\Sigma^+$, $J = 1.5$ for $A\,^2\Pi$ and $C\,^2\Pi$, and $J = 1.5$ for $A'\,^2\Delta$ which we consider as a good proxy for the experimental values (J unspecified) due to the minor J dependence of the lifetimes. The good agreement is partly due to the adjustment of the corresponding TDMC to match the corresponding lifetimes as specified above. Our result is the best we could do for a complicated system $D\,^2\Sigma^+$–$X\,^2\Sigma^+$ with a complex diabatic coupling (Fig. 3) and the diabatized $D\,^2\Sigma^+$–$X\,^2\Sigma^+$ TDMC based on some level of arbitrariness (Fig. 7).

9 COMPARISONS TO EXPERIMENTAL SPECTRA

Fig. 15 compares the experimental $A\,^2\Pi_{1/2} \rightarrow X\,^2\Sigma^+$ $v = 0 \rightarrow 0$ emission bands measured by Bernard, Bacis & Luc (1979) via Fourier transform spectroscopy (black, extracted from their fig. 2) to our computed spectra (red). We simulate our spectra at the temperature of 1500 K to agree with the rotational structure of the experiment. We see excellent agreement in both line position and band structure with the experiment. Some discrepancies can be seen in the line intensities, but this could be due to our assumptions about the

temperature and line broadening. Table 5 provides an extended comparisons of the positions of band heads of the $A\,^2\Pi$–$X\,^2\Sigma^+$ system between the experimental values reported by Bernard & Gravina (1983) and the theoretical values from the present work, as well as the corresponding values of $J_{\rm head}$. Generally, the magnitude of residuals $\Delta\tilde{\nu} = \tilde{\nu}_{\rm exp} - \tilde{\nu}_{\rm calc}$ correlates with the level of the rotational and vibrational excitations. The band heads with $J_{\rm head}$ below 70.5 and $v \leq 8$ agree within $\sim$0.1 cm^{-1}, which then degrades to about 0.5 cm^{-1} for $J_{\rm head} \rightarrow 100.5$.

As in Smirnov et al. (2019), for the sake of completeness, we provide comparisons with the emission $A'^2\Delta - X^2\Sigma^+$ spectrum from Simard et al. (1992), Fig. 16, and the $B\,^2\Sigma^+ - X\,^2\Sigma^+$ and $D\,^2\Sigma^+ - X\,^2\Sigma^+$ absorption spectrum from Zhang et al. (2017), Fig. 17 using the BRYTS line list, now with an improved agreement, see also the corresponding discussions in Smirnov et al. (2019). Figure 16 shows the simulation of the forbidden band *A'*-*X* (0,0) in emission at $T = 77$ K. In Fig. 17, non-local thermodynamic equilibrium conditions with the rotational temperature $T_{\rm rot} = 50$ K and the vibrational temperature of $T_{\rm vib} = 800$ K to better reproduce the experimental spectrum were assumed.

10 CONCLUSIONS

Accurate and extensive empirical BRYTS line lists for ^{89}Y^{16}O, ^{89}Y^{17}O, and ^{89}Y^{18}O are produced covering six lowest doublet electronic states and ranging up to 60 000 cm^{-1}. The line list is based on a refined set of curves in the diabatic representation obtained by fitting to a set of experimentally derived rovibronic energies of YO. The latter is based on the experimental data from the literature, either original laboratory line positions whenever available or spectroscopic constants. Using an effective Hamiltonian to reconstruct molecular energies in place of the original experimental data is less than ideal as it lacks information on any local perturbations, which is critical when using it to fit the spectroscopic model.

Although ExoMol line lists, including BRYTS, are usually intended for astrophysical applications for hot atmospheric environments, YO is one of the molecules used in cooling applications, where our line list may also be useful.

The *ab initio* calculations, especially MRCI, of transition metal species are still a big challenge and therefore ultimately the experimental data (transition frequencies, intensities, dipoles, and lifetimes) are crucial source of the information to produce useful line lists. For YO, we were lucky to have the *ab initio* PECs of excited electronic states of the CCSD(T) quality, while everything else had to rely on the fit to the experiment.

In this work, the hyperfine structure of the YO rovibronic states was ignored, mostly due to the lack of experimental data. Should it become important for YO spectroscopic applications to include the hyperfine effects, the methodology to compute the hyperfine-resolved energies and spectra is readily available as implemented in DUO (Qu, Yurchenko & Tennyson 2022a, b; Bowesman, Yurchenko & Tennyson 2023).

ACKNOWLEDGEMENTS

We thank Amanda Ross for extremely valuable advice on the effective rotational Hamiltonian in connection with the $A\,^2\Pi$-$X\,^2\Sigma^+$ data by Bernard et al. (1979). Her help led to huge improvement of our $A\,^2\Pi$ state model and in the associated quality of the line list. This work was supported by the European Research Council (ERC) under the European Union's Horizon 2020 research and innovation programme through advance grant number 883830 and the STFC projects no. ST/M001334/1 and ST/R000476/1. The authors acknowledge the use of the Cambridge Service for Data Driven Discovery (CSD3) as part of the STFC DIRAC HPC Facility (www.dirac.ac.uk), funded by BEIS capital funding via STFC capital grants ST/P002307/1 and ST/R002452/1 and STFC operations grant ST/R00689X/1. ANS and VGS acknowledge support from project no. FZZW-2023-0010.

DATA AVAILABILITY

The states, transition, opacity, and partition function files for the YO line lists can be downloaded from www.exomol.com. The open access programs DUO and EXOCROSS are available from github.com/exomol.

REFERENCES

Ackermann R. J., Rauh E. G., 1974, J. Chem. Phys., 60, 2266
Al-Refaie A. F., Changeat Q., Waldmann I. P., Tinetti G., 2021, ApJ, 917, 37
Bacis R., Cerny D., D'Incan J., Guelachvili G., Roux F., 1977, ApJ, 214, 946
Badie J. M., Granier B., 2002, Chem. Phys. Lett., 364, 550
Badie J. M., Granier B., 2003, Eur. Phys. J.–Appl. Phys, 21, 239
Badie J. M., Cassan L., Granier B., 2005a, Eur. Phys. J.–Appl. Phys, 29, 111
Badie J. M., Cassan L., Granier B., 2005b, Eur. Phys. J.–Appl. Phys, 32, 61
Badie J. M., Cassan L., Granier B., 2007a, Eur. Phys. J.–Appl. Phys, 38, 177
Badie J. M., Cassan L., Granier B., Florez S. A., Janna F. C., 2007b, J. Sol. Energy Eng. Trans.–ASME, 129, 412
Bagare S. P., Murthy N. S., 1982, Pramana, 19, 497
Barklem P. S., Collet R., 2016, A&A, 588, A96
Bernard A., Gravina R., 1980, ApJS, 44, 223
Bernard A., Gravina R., 1983, ApJS, 52, 443
Bernard A., Bacis R., Luc P., 1979, ApJ, 227, 338
Bowesman C. A., Yurchenko S. N., Tennyson J., 2023, Mol. Phys.
Brady R. P., Yurchenko S. N., Kim G.-S., Somogyi W., Tennyson J., 2022, Phys. Chem. Chem. Phys., 24, 24076
Brady R. P., Drury C., Tennyson J., Yurchenko S. N., 2023, J. Chem. Theory Comput., submitted
Brown J. M., Merer A. J., 1979, J. Mol. Spectrosc., 74, 488
Cazzoli G., Cludi L., Puzzarini C., 2006, J. Mol. Struct., 780-81, 260
Chalek C. L., Gole J. L., 1976, J. Chem. Phys., 65, 2845
Chalek C. L., Gole J. L., 1977, Chem. Phys., 19, 59
Childs W. J., Poulsen O., Steimle T. C., 1988, J. Chem. Phys., 88, 598
Chubb K. L. et al., 2021, A&A, 646, A21
Collopy A. L., Hummon M. T., Yeo M., Yan B., Ye J., 2015, New J. Phys, 17, 055008
Collopy A. L., Ding S., Wu Y., Finneran I. A., Anderegg L., Augenbraun B. L., Doyle J. M., Ye J., 2018, Phys. Rev. Lett., 121, 213201
Dye R. C., Muenchausen R. E., Nogar N. S., 1991, Chem. Phys. Lett., 181, 531
Fried D., Kushida T., Reck G. P., Rothe E. W., 1993, J. Appl. Phys., 73, 7810
Furtenbacher T., Császár A. G., Tennyson J., 2007, J. Mol. Spectrosc., 245, 115
Goranskii V. P., Barsukova E. A., 2007, Astron. Rep., 51, 126
Hoeft J., Torring T., 1993, Chem. Phys. Lett., 215, 367
Hulburt H. M., Hirschfelder J. O., 1941, J. Chem. Phys., 9, 61
Irwin P. G. J. et al., 2008, J. Quant. Spectrosc. Radiat. Transfer, 109, 1136
Kaminski T., Schmidt M., Tylenda R., Konacki M., Gromadzki M., 2009, ApJS, 182, 33
Kasai P. H., Weltner W., Jr, 1965, J. Chem. Phys., 43, 2553
Knight L. B., Kaup J. G., Petzoldt B., Ayyad R., Ghanty T. K., Davidson E. R., 1999, J. Chem. Phys., 110, 5658
Kobayashi T., Sekine T., 2006, Chem. Phys. Lett., 424, 54
Langhoff S. R., Bauschlicher C. W., 1988, J. Chem. Phys., 89, 2160

Lee E. G., Seto J. Y., Hirao T., Bernath P. F., Le Roy R. J., 1999, J. Mol. Spectrosc., 194, 197
Leung J. W. H., Ma T. M., Cheung A. S. C., 2005, J. Mol. Spectrosc., 229, 108
Linton C., 1978, J. Mol. Spectrosc., 69, 351
Liu K., Parson J. M., 1977, J. Chem. Phys., 67, 1814
Liu K., Parson J. M., 1979, J. Phys. Chem., 83, 970
Manos D. M., Parson J. M., 1975, J. Chem. Phys., 63, 3575
Medvedev E. S., 2012, J. Chem. Phys., 137, 174307
Medvedev E. S., Ushakov V. G., 2022, J. Quant. Spectrosc. Radiat. Transfer, 288, 108255
Medvedev E. S., Meshkov V. V., Stolyarov A. V., Gordon I. E., 2015, J. Chem. Phys., 143, 154301
Medvedev E. S., Meshkov V. V., Stolyarov A. V., Ushakov V. G., Gordon I. E., 2016, J. Mol. Spectrosc., 330, 36
Min M., Ormel C. W., Chubb K., Helling C., Kawashima Y., 2020, A&A, 642, A28
Molliére P., Wardenier J. P., van Boekel R., Henning T., Molaverdikhani K., Snellen I. A. G., 2019, A&A, 627, A67
Mukund S., Nakhate S. G., 2023, J. Quant. Spectrosc. Radiat. Transfer, 296, 108452
Murty P. S., 1982, Astrophys. Lett., 23, 7
Murty P. S., 1983, Astrophys. Space Sci., 94, 295
Otis C. E., Goodwin P. M., 1993, J. Appl. Phys., 73, 1957
Peterson K. A., Dunning T. H., 2002, J. Chem. Phys., 117, 10548
Peterson K. A., Figgen D., Dolg M., Stoll H., 2007, J. Chem. Phys., 126, 124101
Prajapat L., Jagoda P., Lodi L., Gorman M. N., Yurchenko S. N., Tennyson J., 2017, MNRAS, 472, 3648
Qu Q., Yurchenko S. N., Tennyson J., 2022a, J. Chem. Theory Comput., 18, 1808
Qu Q., Yurchenko S. N., Tennyson J., 2022b, J. Chem. Phys., 157, 124305
Quéméner G., Bohn J. L., 2016, Phys. Rev. A, 93, 012704
Sauval A. J., 1978, A&A, 62, 295
Semenov M., Yurchenko S. N., Tennyson J., 2016, J. Mol. Spectrosc., 330, 57
Shin J. B., Nicholls R. W., 1977, Spectr. Lett., 10, 923
Shu Y., Varga Z., Kanchanakungwankul S., Zhang L., Truhlar D. G., 2022, J. Phys. Chem. A, 126, 992
Simard B., James A. M., Hackett P. A., Balfour W. J., 1992, J. Mol. Spectrosc., 154, 455
Smirnov A. N., Solomonik V. G., Yurchenko S. N., Tennyson J., 2019, Phys. Chem. Chem. Phys., 21, 22794
Steimle T. C., Alramadin Y., 1986, Chem. Phys. Lett., 130, 76
Steimle T. C., Alramadin Y., 1987, J. Mol. Spectrosc., 122, 103
Steimle T. C., Shirley J. E., 1990, J. Chem. Phys., 92, 3292
Steimle T. C., Virgo W., 2003, J. Mol. Spectrosc., 221, 57
Suenram R. D., Lovas F. J., Fraser G. T., Matsumura K., 1990, J. Chem. Phys., 92, 4724
Tennyson J., Yurchenko S. N., 2012, MNRAS, 425, 21
Tennyson J., Hill C., Yurchenko S. N., 2013, in AIP Conf. Proc. Vol. 1545, 8th International Conference on Atomic and Molecular Data and their Applications (ICAMDATA-2012). AIP, New York, p. 186
Tennyson J. et al., 2020, J. Quant. Spectrosc. Radiat. Transfer, 255, 107228
Tylenda R., Górny S. K., Kamínski T., Schmidt M., 2015, A&A, 578, A75
Uhler U., Akerlind L., 1961, Ark. Fys., 19, 1
Ushakov V. G., Semenov M., Yurchenko S. N., Ermilov A. Y., Medvedev E. S., 2023, J. Mol. Spectrosc., 395, 111804
Vardya M. S., 1970, A&A, 5, 162
Werner H.-J. et al., 2020, J. Chem. Phys., 152, 144107
Western C. M., 2017, J. Quant. Spectrosc. Radiat. Transfer, 186, 221
Wijchers T., Dijkerman H. A., Zeegers P. J. T., Alkemade C. T. J., 1980, Spectra Chim. Acta B, 35, 271
Wijchers T., Dijkerman H. A., Zeegers P. J. T., Alkemade C. T. J., 1984, Chem. Phys., 91, 141
Wyckoff S., Clegg R. E. S., 1978, MNRAS, 184, 127
Yeo M., Hummon M. T., Collopy A. L., Yan B., Hemmerling B., Chae E., Doyle J. M., Ye J., 2015, Phys. Rev. Lett., 114, 223003
Yurchenko S. N., Lodi L., Tennyson J., Stolyarov A. V., 2016, Comput. Phys. Commun., 202, 262
Yurchenko S. N., Sinden F., Lodi L., Hill C., Gorman M. N., Tennyson J., 2018a, MNRAS, 473, 5324
Yurchenko S. N., Al-Refaie A. F., Tennyson J., 2018b, A&A, 614, A131
Yurchenko S. N., Nogué E., Azzam A. A. A., Tennyson J., 2022, MNRAS, 520, 5183
Zhang D., Zhang Q., Zhu B., Gu J., Suo B., Chen Y., Zhao D., 2017, J. Chem. Phys., 146, 114303

SUPPORTING INFORMATION

Supplementary data are available at *MNRAS* online.

This includes (i) the spectroscopic model in the form of the DUO input file, containing all the curves, parameters as well as the experimentally derived energy term values of YO used in the fit; (ii) the experimental line positions collected from the literature in the MARVEL format, and (iii) an effective Hamiltonian for a $^2\Pi$ electronic state from Bacis et al. (1977).

Please note: Oxford University Press is not responsible for the content or functionality of any supporting materials supplied by the authors. Any queries (other than missing material) should be directed to the corresponding author for the article.

This paper has been typeset from a TEX/LATEX file prepared by the author.